Journal of Power Sources 374 (2018) 61–68

Contents lists available at ScienceDirect

Journal of Power Sources

journal homepage: www.elsevier.com/locate/jpowsour

Quantification of the degradation of Ni-YSZ anodes upon redox cycling

Bowen Song*, Enrique Ruiz-Trejo, Antonio Bertei, Nigel P. Brandon

Department of Earth Science and Engineering, Imperial College London, United Kingdom

HIGHLIGHTS

- Quantification of redox damage by coupling 3D tomography, EIS and nanoindentation.
- YSZ fracture, Ni detachment and agglomeration led to irreversible mechanical damage.
- Ni nanoparticles obtained upon redox cycling improve electrochemical performance.
- Loss in TPB density estimated by model matches 3D FIB-SEM data.

ARTICLE INFO

Keywords:
Anode degradation
Tomography
Electrochemical impedance spectroscopy
Nanoindentation

ABSTRACT

Ni-YSZ anodes for Solid Oxide Fuel Cells are vulnerable to microstructural damage during redox cycling leading to a decrease in the electrochemical performance. This study quantifies the microstructural changes as a function of redox cycles at 800 °C and associates it to the deterioration of the mechanical properties and polarisation resistance. A physically-based model is used to estimate the triple-phase boundary (TPB) length from impedance spectra, and satisfactorily matches the TPB length quantified by FIB-SEM tomography: within 20 redox cycles, the TPB density decreases from 4.63 μm^{-2} to 1.06 μm^{-2}. Although the polarisation resistance increases by an order of magnitude after 20 cycles, after each re-reduction the electrode polarisation improves consistently due to the transient generation of Ni nanoparticles around the TPBs. Nonetheless, the long-term degradation overshadows this transient improvement due to the nickel agglomeration. In addition, FIB-SEM tomography reveals fractures along YSZ grain boundaries, Ni-YSZ detachment and increased porosity in the composite that lead to irreversible mechanical damage: the elastic modulus diminishes from 36.4 GPa to 20.2 GPa and the hardness from 0.40 GPa to 0.15 GPa. These results suggest that microstructural, mechanical and electrochemical properties are strongly interdependent in determining the degradation caused by redox cycling.

1. Introduction

The solid oxide fuel cell (SOFC) is currently one of the most promising energy conversion devices, offering a high operating efficiency with minimal air pollution. Ni-YSZ cermets are the most commonly used SOFC anode materials, offering a combination of relatively low cost and good performance. However, the material can degrade when subject to certain operating conditions, such as redox cycling during operation [1–5].

Past work has often concentrated on Ni-YSZ microstructural evolution by annealing for long periods of time. It is commonly agreed that under these conditions the accompanying performance loss is caused by an increase in average Ni particle size and a decrease in active triple phase boundary (TPB) length per unit volume. The active TPB is the theoretical contact perimeter between percolating Ni, YSZ and pore phase, where fuel oxidation and charge transfer occur [6–8]. Ni-YSZ anodes are typically fabricated by mixing YSZ and NiO particles, which are subsequently reduced by H_2 during the fuel cell start-up. Reduction of the NiO–YSZ involves a quasi-reversible dimensional shrinkage of 41.6% by converting NiO to Ni. However, Ni is strongly sensitive to oxidising atmospheres, such as those present during operation at high fuel conversion or during emergency shut-down, which can rapidly convert Ni into its oxidised state, involving a 71.2% volume expansion. These Ni volume changes result in irreversible microstructural damage, which include bulk deformation of the microstructure, commonly leading to electrolyte cracking [1,2,9]. The size changes of Ni particles were suggested to be due to the agglomeration of metallic nickel [10] and the formation of porosity upon reduction [11]. These parameters also show a direct relationship with the change of the effective TPB length [7]. The increase in Ni particle size could lead to a corresponding drop of TPB density and growth of polarisation resistance [12], moreover, due to the potential loss of Ni–Ni contact, the electrical

* Corresponding author.
E-mail address: b.song15@imperial.ac.uk (B. Song).

https://doi.org/10.1016/j.jpowsour.2017.11.024
Received 17 August 2017; Received in revised form 17 October 2017; Accepted 7 November 2017
0378-7753/ © 2017 The Authors. Published by Elsevier B.V. This is an open access article under the CC BY license (http://creativecommons.org/licenses/BY/4.0/).

conductivity can decrease as well.

Focused ion beam (FIB)-SEM tomography [13,14] allows the microstructural change seen in Ni-YSZ electrodes after redox cycling to be quantified through ex-situ analysis, due to the good phase contrast between Ni and YSZ, and the relatively high resolution of the technique. From the 3D tomography reconstructed microstructure, parameters such as volume fractions, interfacial areas, TPB length and tortuosity factors can be quantified [9,15–19]. In terms of electrochemical performance, electrochemical impedance spectroscopy (EIS) is commonly used, as it is an effective technique to follow electrochemical changes in real time [20–22]. It has been found that after redox cycling, polarisation resistance increased due to TPB length reduction and Ni surface area decrease [5,9,19]. The relationship between electrode microstructure properties and electrochemical impedance response has been recently quantified by Bertei et al. [24], using a physically-based model [25,26].

Knowledge of the behaviour of Ni-YSZ is also important for the mechanical design of the SOFC. The mechanical properties of Ni-YSZ have been widely studied with a wide range of techniques. The Impulse Excitation Technique (IET) was used to determine parameters in thick Ni-YSZ electrodes, 300 μm or above, comparing elastic modulus with porosity, Ni content and sintering temperature [1,27–29]. The empirical relationship of porosity and elastic modulus of Ni-YSZ has been reported and validated in several studies [29,30]. A comparison of different mechanical properties determined by these experimental techniques has been undertaken [31]. The nanoindentation technique has been developed and used to study the response of the material at smaller length scales [32,33]. However, there is currently no study available on the nanoindentation characterisation of the micromechanical properties of porous Ni-YSZ films upon redox cycling.

This paper presents an integrated study of the impact of redox cycling on the microstructure, electrochemical performance and mechanical properties of porous Ni-YSZ cermets, using a variety of methods such as 3D tomography, nanoindentation, EIS and modelling to develop an improved understanding of the coupled nature of anode behaviour under such redox cycling conditions.

2. Experimental

2.1. Fabrication of NiO-YSZ cell

Ni-YSZ symmetrical cells were prepared with a NiO-YSZ slurry made from NiO and YSZ powder (Nexceris, USA, 60 wt% NiO, 2.45 $m^2 g^{-1}$ surface area) mixed with terpineol, binder (Hercules ECN-7) and dispersant (Hypermer KD15). A ceramic triple-roll mill was used to homogenise the slurry and eliminate agglomerates above 5 μm. The slurry was deposited by tape casting on an 8YSZ electrolyte (Nexceris, USA, Ø = 2 cm, 250–300 μm) and fired at 1200 °C for 2 h in air. The final electrodes had a thickness of 25–30 μm and 2 cm^2 geometric surface area.

2.2. Redox cycling

Redox cycling was carried out by sequentially exposing the cell to two different gas streams, air and diluted hydrogen (a mixture of 5 vol % H_2 and 95 vol % N_2), both humidified with 3% vol H_2O, with a flush of N_2 in between. The process was carried out at 800 °C within a quartz tube furnace. For each redox cycle, the samples were kept in air for 1 h, flushed for 10 min in N_2 and then reduced in H_2 for approximately 5 h, as schematically reproduced in Fig. 1. This procedure, already adopted by Shimura et al. [9], rather than mimicking any specific accidental or emergency situation, represents a benchmark scenario for reproducible redox cycling measurements around the typical working condition of an SOFC.

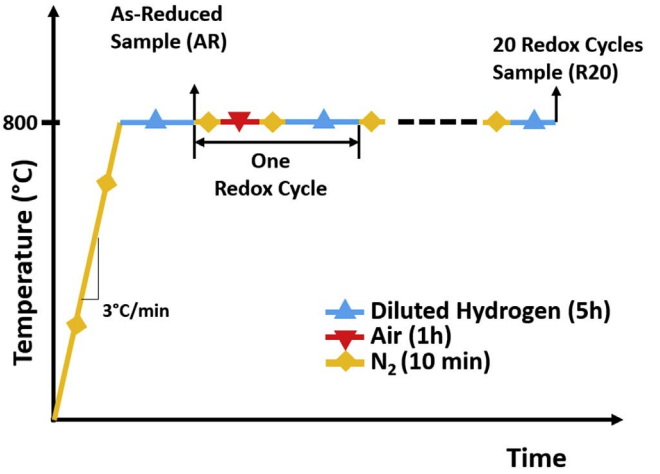


Fig. 1. Representation of redox cycling procedure. Impedance spectra were taken during each reduction process as a function of time.

2.3. Characterisation procedure

EIS measurements were performed within a frequency range of 10^6Hz-10^{-1} Hz with 20 mV AC amplitude using a potentiostat (Autolab PGSTAT302N), every 30 min during the reduction process in diluted hydrogen atmosphere. The measurement data were fitted to an equivalent electrical circuit, shown in Fig. 2, by using ZView3.5 (Scribner Associates Incorporated). The active TPB density was estimated from the intermediate-frequency polarisation resistance R_2 using a validated physically-based model [24], as follows:

$$R_2 = 2\frac{t_{an}}{k_{eff}\sigma_{io}}\frac{coth(\Gamma)}{\Gamma} \quad (1)$$

$$\Gamma = t_{an}\sqrt{\frac{F}{RT}\frac{i_0 L_{TPB}}{k_{eff}\sigma_{io}}} \quad (2)$$

where the factor 2 represents the two electrodes for the symmetric cell, t_{an} is the anode thickness, F the Faraday constant, R the gas constant, T the operating temperature in K, k_{eff} is the effective conductivity factor

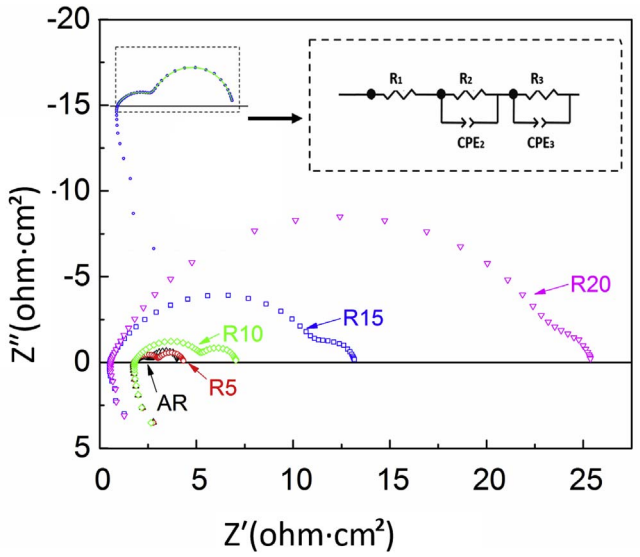


Fig. 2. Impedance spectra recorded after 0, 5, 10, 15, 20 redox cycles at 800 °C, 2 h after the introduction of wet 5 vol % H_2, AR represents as-reduced, R5 represents 5 redox cycles, R10 10 redox cycles and so on. The inset shows equivalent circuit fitting result. R_1, R_2, R_3 represent the high-frequency intercept resistance, intermediate frequency resistance and low-frequency resistance respectively; CPE_2, CPE_3 represent constant phase element for the corresponding frequency[28].

of the YSZ phase, σ_{io} is the ionic conductivity of YSZ, i_0 is the exchange current density per unit of TPB length calculated according to Bieberle et al. correlation [34], L_{TPB} is the active TPB density per unit of electrode volume. Electronic ohmic losses were omitted because proved to be negligible as long as Ni phase percolates [24,35], the parameters k_{eff}, i_0, σ_{io} and YSZ volume fraction used in this simulation were assumed to be constant with time during reduction and equal to the as-reduced conditions. It is assumed that polarisation degradation is caused solely by a decrease in TPB density [24]. L_{TPB} can be evaluated by using Eqs. (1) and (2) from the polarisation resistance R_2 measured with EIS [24].

A scanning electron microscope (LEO, Gemini 1525 FEGSEM) was used to study the surface and cross-sectional microstructure of samples before and after redox cycling. Tomography was used to gain insight into the resultant microstructural changes, using a FIB-SEM dual-beam instrument (Auriga Cross Beam, Zeiss) for 3D reconstruction. The cross-section of the anode was repeatedly milled by FIB and observed by SEM with approx. 25 nm between each slice. The series of FIB-SEM images were processed and segmented in Avizo 9.0.0 image processing software (Visualization Science Group, Mérignac, France) and the 3D microstructure of Ni–YSZ samples was reconstructed.

The porosity, surface areas and active TPB density were evaluated from the segmented 3D datasets. The tortuosity and effective conductivity factor of the YSZ and Ni phases were calculated using the open source Matlab application TauFactor [36]. All the calculations were made on a voxel-basis. This advanced characterisation allowed for the quantification of microstructure parameter changes between samples after redox cycling.

The mechanical properties of five samples after 0(AR), 5(R5), 10(R10), 15(R15) and 20(R20) redox cycles were measured by nanoindentation (NanoTest Platform, Micromaterial, UK) at room temperature. A sharp tip was indented into the material surface and the material response during the loading and unloading was recorded. Over 200 indentations per sample were carried out with a Vickers diamond tip with a 200 μm interval to obtain a statistically representative dataset and avoid outliers due to inhomogeneities.

The elastic modulus, E, and hardness, H, were calculated from the load–depth curves using Oliver–Pharr analysis:

$$E = \frac{1 - \nu^2}{\frac{1}{M} - \frac{1-\nu_i^2}{E_i}} \quad (3)$$

$$M = \frac{\beta}{2}\left(\frac{dp}{dh}\sqrt{\frac{\pi}{A}}\right) \quad (4)$$

$$H = \frac{P_{max}}{A} \quad (5)$$

where ν is the Poisson's ratio of the specimen, which is 0.387 approximately [37]; E_i and ν_i are the elastic modulus = 1220 GPa and Poisson's ratio = 0.07 of the diamond indenter, respectively; M is the indentation modulus, β is a geometrical correction factor, which is 1.055 for a Vickers diamond tip [38]; P_{max} is the maximum load applied and A is the contact area between indenter and material, which is, $A = 4h_c^2 tan^2 68^o = 24.504 h_c^2$ for a Vickers indenter, where h_c is the indentation loading depth.

3. Results and discussion

3.1. Electrochemical degradation on redox cycling

The electrochemical degradation of the cell was quantified by measuring the impedance upon introduction of hydrogen during the redox cycles. Five selected redox cycles are presented in Fig. 2: a minor change of ohmic resistance (R_1), a significant increase in polarisation resistance (R_2) and a relatively steady diffusion resistance (R_3) are observed. This is consistent with work performed by Laurencin et al. [28]. The inset shows an example of fitting with the equivalent circuit,

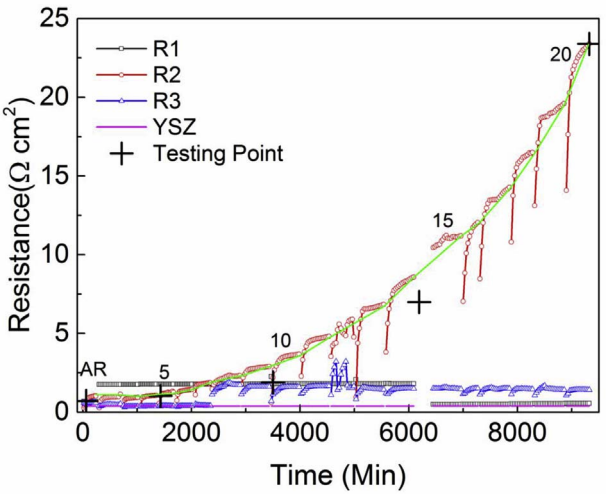


Fig. 3. Resistances as a function of time during the reduction process of redox cycling as from EIS fitting. The solid green line is a guide to the degradation trend. The cross marks represent the time scale of the samples used for 3D tomography reconstruction. (For interpretation of the references to colour in this figure legend, the reader is referred to the web version of this article.)

performed within the frequency range 10^6–10^{-1} Hz.

Fig. 3 presents the resistances extracted from the fitting. The ohmic resistance (R_1) shows a relatively steady performance during 20 redox cycles, apart from a sharp improvement after 14 cycles and a uniform performance afterwards. This corroborates that there has not been a significant degradation of R_1, which mainly reflects the resistance of the YSZ electrolyte, which is 0.393 Ωcm^2 based on a calculation for a 250 μm thick YSZ pellet, with 2 cm [2] area at 800 °C [39]. Not surprisingly the measured ohmic resistance is higher than the calculated electrolyte ionic resistance (compare black squares with the pink line in the lower section of Fig. 3) as the measured ohmic resistance takes into account additional interfacial and electrode ohmic losses. An improvement in contact resistance between anode surface and Pt mesh may be responsible for the sharp change in R_1 observed at cycle 15. The diffusion resistance (R_3) is attributed to losses by gas conversion and gas diffusion [5] occurring outside the porous electrode microstructure [24], the minor change after cycle 8 may be caused by accidental rig movements during the testing. Notably, R_1 and R_3 show sudden changes only, which are uncorrelated from the change in R_2. Finally, the polarisation resistance (R_2) shows in general a continuous increase after redox cycling. Changes in R_2 are mostly considered to be related to charge transfer and the activation overpotential of the fuel oxidation process at the TPB as observed also in Ni-infiltrated scaffolds [26]. As pointed out by Laurencin et al. [28], the characteristic frequency associated to R_2 remained relatively constant upon redox cycling, suggesting that the increase in R_2 could be due to a mechanical damage along the electrochemical interfaces, that is, to a loss in effective TPB length. Another interesting feature is that, within each reduction process, R_2 shows a good initial value followed by a rapid degradation before approaching a more stable value, similar to observations by Shimura et al. [9] in cermet anodes as well as by Bertei et al. in nanostructured anodes [26]. By comparing between two adjacent cycles, it appears that R_2 shows significant performance improvement at the start of a new reduction process. This phenomenon suggests that the reduction of the NiO leads to a significant increase in TPB density at the initial stage, but as the annealing proceeds, the TPB length reaches a more stable level. Bertei et al. suggested this might be due to the rapid evolution of the nanometric roughness of Ni surface generated in-situ during the reduction process [26].

A physically-based model was used to estimate the active TPB density from the evolution of R_2, under the assumption that the electrochemical performance changes are directly linked to the TPB density

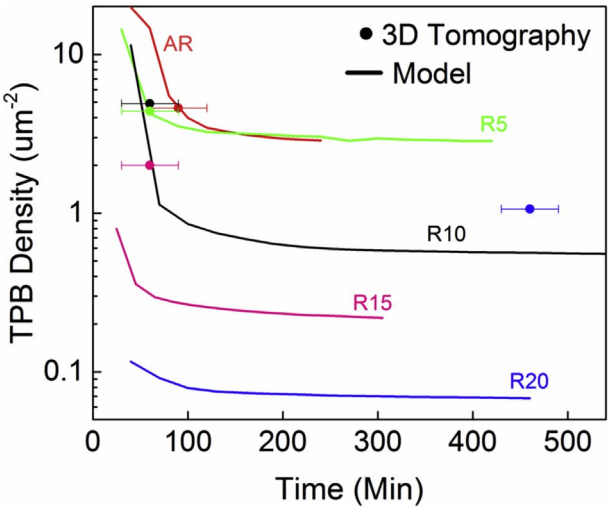


Fig. 4. Active TPB density vs time for different redox cycles as determined from 3D tomography (symbols) and EIS modelling (line). The error bars refer to the uncertainty in positioning the time scale of the reconstructed samples, due to the cooling time of the samples. Note that, differently from other samples, sample R20 refers to the end of the annealing time.

only [24]. Fig. 4 shows the TPB density estimated by the electrochemical model for the as-reduced sample and after 5, 10, 15 and 20 redox cycles. These data points are compared with the active TPB density evaluated from tomographic reconstruction at selected points. Within any redox cycle, the model predicts a fast decrease in TPB density within 2 h, followed by stabilisation. The Ni surface roughness and nanoparticles observed using SEM (see next section) may contribute significantly to the TPB evolution. Although not exhaustively proved yet, it could be proposed that, at an early stage, NiO-Ni deformation or asymmetrical reduction processes lead to a rough surface [26] and generate a large number of Ni nanoparticles [40]. This surface roughness and the nanoparticles attached to the percolating Ni and YSZ frameworks can lead to a significant increase in TPB density. However, these features start to agglomerate with other Ni particles or form volatile Ni species [41], resulting in a subsequent rapid drop in TPB density. This rapid evolution of TPB density has also been reported in nano-infiltrated anodes [25,26]. For the samples with more redox cycles, the initial degradation tends to be slower, as Ni particles are comparatively bigger (see next section). Overall, after stabilisation, the TPB density of samples shows a decreasing trend versus redox cycle number. This may be caused by Ni agglomeration during the overall redox cycling process.

The comparison of the active TPB density between FIB-SEM tomography and the model prediction shows a good consistency for the AR, R5 and R10 samples, see Fig. 4. For the samples after 15 and 20 redox cycles, as the number of redox cycles increases, the difference between the 3D tomography data and the electrochemical model values increases. This is because the complex microstructural changes caused by redox cycling may not all be detected by 3D tomography since Ni nanoparticles, nano surface roughness and cracks may be beyond the resolution level, as shown in Fig. 5 and extensively discussed by Bertei et al. [26]. Moreover, the electrochemical model attributes all the degradation to the decrease in TPB density, while cracks in the YSZ framework would reduce the effective ionic conductivity, which is considered constant in the model. Thus, the discrepancy of values for R15 and R20 suggests that the YSZ cracks, generated during redox cycling, led to a decrease in the effective ionic conductivity, not considered by the electrochemical model.

3.2. Microstructural characterisation on redox cycling

The microstructural characterisation was carried out with both SEM image analysis and 3D tomography reconstruction. Five different samples, with various numbers of redox cycles, were tested. The approximate time scale of sample observation points is indicated in Fig. 3 using black crosses.

Fig. 5 shows the SEM image of the Ni-YSZ electrode. In the as-reduced sample (a), detachment between Ni and YSZ particles is observed as a consequence of Ni volume shrinkage after reduction. The bottom two images show the SEM top surfaces of redox cycled samples. Ni particle agglomeration is observed, that could result in porosity increase. More interestingly, a growing number of Ni nanoparticles appeared on the Ni surface and at the boundary between Ni and YSZ. In addition, no impurities were noticed beyond the detection limits of energy dispersive X-ray spectroscopy (EDX). This is consistent with the Ni microstructure change reported by Hanasaki et al. [3]. The Ni nanoparticles located at the boundary between Ni and YSZ can significantly extend the TPB length, which is consistent with the increase in TPB density seen in the early stage of each reduction process as estimated by the model from the analysis of EIS data (Figs. 3 and 4). In addition to this, cracks are found between YSZ grain boundaries, especially after a large number of redox cycles (> 10). This could be due to the mechanical damage caused by Ni volume expansion during reoxidation, since this type of crack does not appear in the as-reduced samples. By constantly breaking the YSZ grain boundaries around Ni particles, the YSZ framework within the electrode results in smaller isolated regions, thus losing its ionic transport path and supporting function. This contributes to the steady increase in polarisation resistance as well as to the decrease in the material hardness and elastic modulus as discussed in the next section.

The microstructural characterization is complemented by 3D tomographic reconstruction. The middle column of Fig. 6 shows the cross-sectional images from FIB-SEM. The Ni particle (light grey) agglomeration is confirmed here, as well as the trend of the YSZ structure to be broken into smaller pieces, as discussed above. However, due to the limitation of FIB-SEM image resolution, the Ni nanoparticles cannot be detected. This is because the average voxel size of these FIB-SEM images is around 20–25 nm, which is about 2–5 times the diameter of the Ni nanoparticles observed with SEM [26]. The presence of small nanoparticles around the TPB may also cause errors in the microstructural tomographic quantification because the colour of each pixel around the TPB is highly affected by the surrounding Ni nanoparticles, which makes image segmentation harder in redox-cycled samples.

A tomographic microstructural reconstruction was carried out for each sample [42,43]. The original images were segmented into three different colours (Blue: Ni, green: YSZ, grey: pore phase), as shown at the right-hand side of Fig. 6. The calculated microstructural parameters are shown in Table 1. The anode porosity, initially similar to that of anode-supporting layers [44,45], increases with redox cycling, consistent with the previously-reported result from Holzer et al. [46]. In addition, the TPB density decreased as redox cycles are repeated. The Ni surface area per volume decreased after the redox cycles, which corroborates the increase in Ni particle size observed from SEM and FIB-SEM images. The interfacial area between Ni and YSZ also decreased, suggesting that the detachment caused by Ni volume shrinkage during reduction can be one reason for the decrease in effective TPB density. Therefore, the quantitative 3D tomographic analysis confirms the trends detected with SEM analysis regarding Ni agglomeration, loss in TPB density and cracking of the YSZ network upon redox cycling.

3.3. Mechanical properties after redox cycling

The elastic modulus and hardness of each sample were measured by using the nanoindentation technique. The load-depth curve of redox-cycled samples are plotted in Fig. 7- a. In this experiment, the maximum

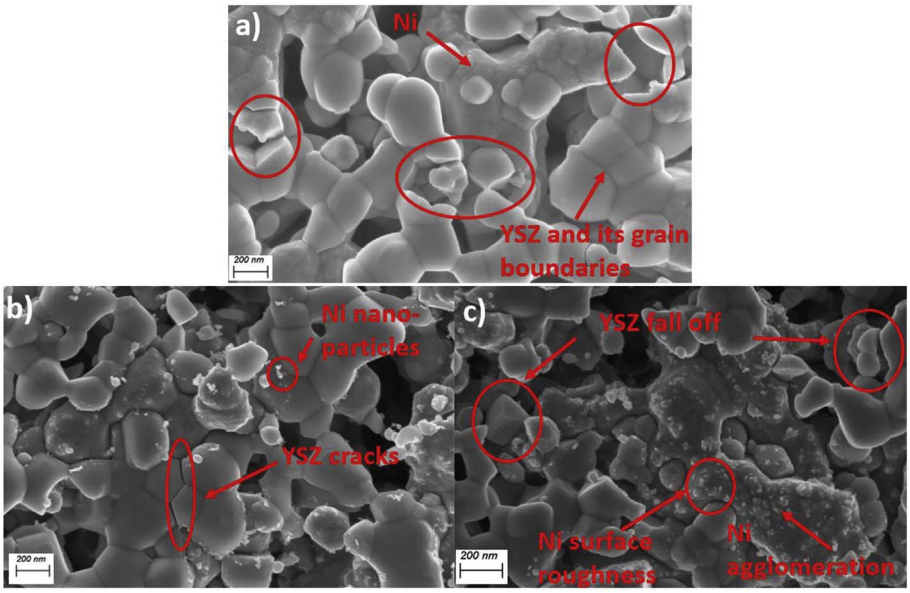


Fig. 5. a) Top-surface SEM images of an as-reduced Ni-YSZ electrode showing the detachment between Ni and YSZ caused by Ni volume shrinkage after reduction, leading to a relatively large space in between; b) Top-surface SEM images of Ni-YSZ electrodes after 5 redox cycles showing the crack along the YSZ grain boundaries, with approximately gap of 10 nm and the Ni nanoparticles c) Top-surface SEM images of Ni-YSZ electrodes after 10 redox cycles showing YSZ grain fall off from its framework and Ni surface roughness, agglomeration along with Ni nanoparticles.

indent load is 115 mN, producing a maximum indentation depth between 3.5 and 5.0 μm. This indentation depth is kept to less than 20% of the electrode thickness (25–30 μm), so that the substrate effect on the measurement is negligible [47]. Having used a symmetric setup rather than an anode-supported configuration makes the electrode constrained on one side by the stiffer YSZ substrate. Thus, the propagation of the mechanical stresses, internally generated within the anode by redox cycling, affects mainly the anode itself, without causing cracking of the YSZ electrolyte and subsequent stress relaxation. Therefore, the symmetric setup allows for the focusing on the intrinsic mechanical behaviour of the porous anode alone, although the stiffness of the thick YSZ electrolyte may slightly amplify the internal anode cracking if

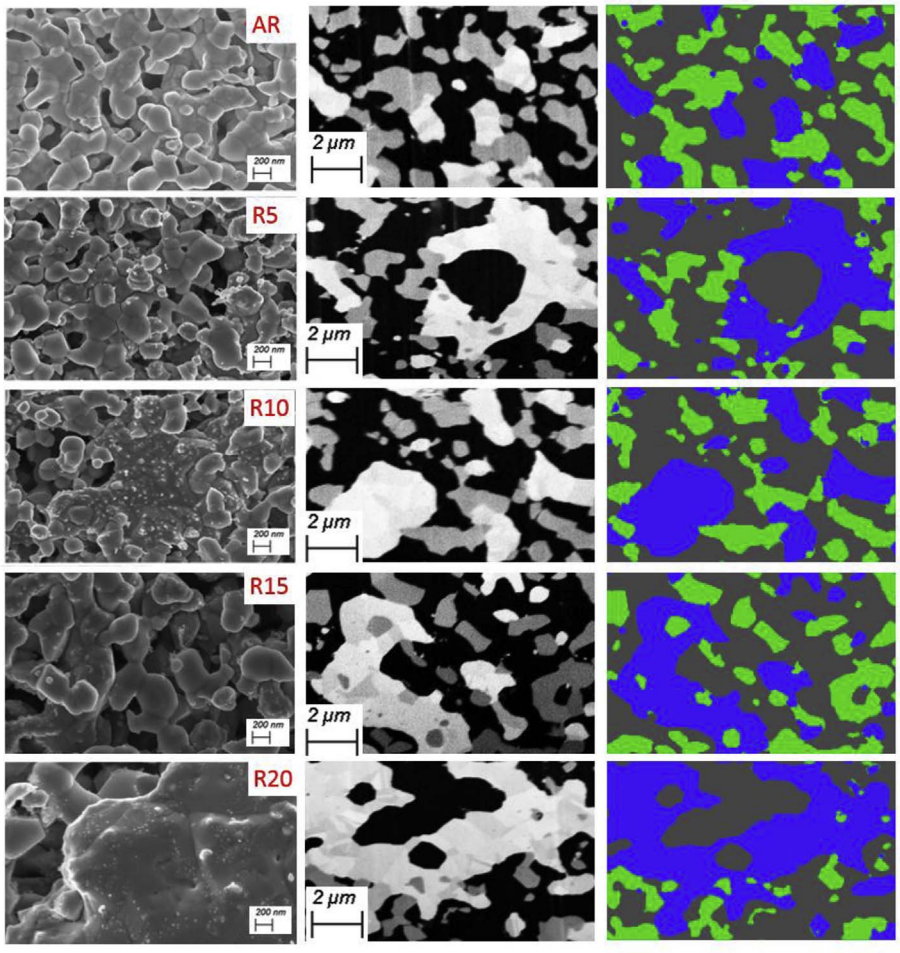


Fig. 6. Left: SEM images of five redox cycled samples. Middle: FIB-milled cross-sectional micrographs of Ni − YSZ anodes after different redox cycles. Light grey: Ni, dark grey: YSZ, and black: pore. Right: the segmented images corresponding to the left side. Blue: Ni, green: YSZ, grey: pore. (For interpretation of the references to colour in this figure legend, the reader is referred to the web version of this article.)

Table 1
Calculated microstructure parameters from the reconstructed 3D tomographic datasets of anodes with different numbers of redox cycles.

		AR	R5	R10	R15	R20
POROSITY		0.442	0.516	0.537	0.534	0.571
ACTIVE TPB DENSITY (μm-2)		4.63	4.90	4.40	2.08	1.06
SURFACE AREA PER TOTAL VOLUME (μm^{-1})	Ni	7.90	7.05	5.97	6.42	5.08
	YSZ	3.65	4.22	3.00	3.82	3.04
	Pore	6.19	6.39	5.91	7.54	6.36
INTERFACE AREA PER TOTAL VOLUME (μm^{-1})	Ni-YSZ	2.68	2.44	1.53	1.35	0.88
	Ni-Pore	5.22	4.61	4.44	5.07	4.20
	YSZ-Pore	0.97	1.78	1.47	2.47	2.16

compared to an anode-supported configuration.

The clear shift in the load curves indicates that the samples with more redox cycles display lower hardness since the same loading force results in greater penetration depth. Since the nanoindentation has a strong sensitivity to individual dislocation interactions, oscillations in each loading curve were observed. This is caused by a complex combination of factors, such as mechanical instabilities, development of dislocation networks, and incipient plasticity [19]. The variance of these oscillations shows that the sample with more redox cycles has a steadier loading curve. Probably, the redox cycling promoted the fragmentation of YSZ framework, which simplified the disorder interactions between the Ni-YSZ composite and indenter, as observed from both SEM and FIB-SEM.

Fig. 7-b and c show the nanoindentation results for elastic modulus and hardness of the electrodes as a function of the number of redox cycles. The results show a clear decreasing trend in both the elastic modulus and hardness, accompanied by a different standard deviation which reflects the combined effects of surface roughness, densification and internal structure changes. With different indentation depths, the generally larger scatter in the data might be related to the greater roughness of the films when compared with the bulk samples. Nevertheless, for both the elastic modulus and the hardness, the standard deviation first increases until 10 cycles and then decreases, indicating that more reproducible data were collected after 20 redox cycles. The maximum in data scattering around 10 cycles can be explained by considering the progressive fragmentation of the microstructure in comparison with the indentation depth, which is 3–5 μm. In the as-reduced sample, the microstructure is macroscopically homogeneous, although Ni-dense and YSZ-dense regions are present at the μm scale as evident in Fig. 6, causing a relatively narrow standard deviation. As the number of redox cycles increases to 5 and 10 cycles, cracks separate relatively big and stiff YSZ fragments from softer Ni regions (Fig. 5), thus the microstructure becomes more locally heterogeneous, as revealed by a larger standard deviation in the mechanical properties. As the redox cycling proceeds (i.e., 15 and 20 cycles), the microstructure is fragmented into pieces smaller than the indentation depth (5 μm), so that the mechanical properties appear to be more spatially homogeneous, resulting overall in a lower standard deviation of mechanical properties (Fig. 7).

Fig. 8 shows the measured Ni-YSZ elastic modulus versus porosity compared with two empirical fitting formulas. The black dashed line represents a linear fitting of porous Ni-YSZ samples prepared by varying the porosity by changing the reduction temperature between 600 and 1000 °C as reported in the literature [29]. The blue dashed line shows an exponential fitting of a porous tape cast Ni-YSZ electrode, sintered at 1400 °C in air for 2 h, as reported by Radovic et al. [27]. The dense elastic modulus values E_0 and porosity constants b are listed in Table 2. While the data points obtained in this study (red symbols) cannot be fitted by a linear correlation, the exponential equation allows for a good fitting once the porosity constant is increased to $b^* = 3.813$ (see the red dashed line in Fig. 8). This increase in porosity constant could be

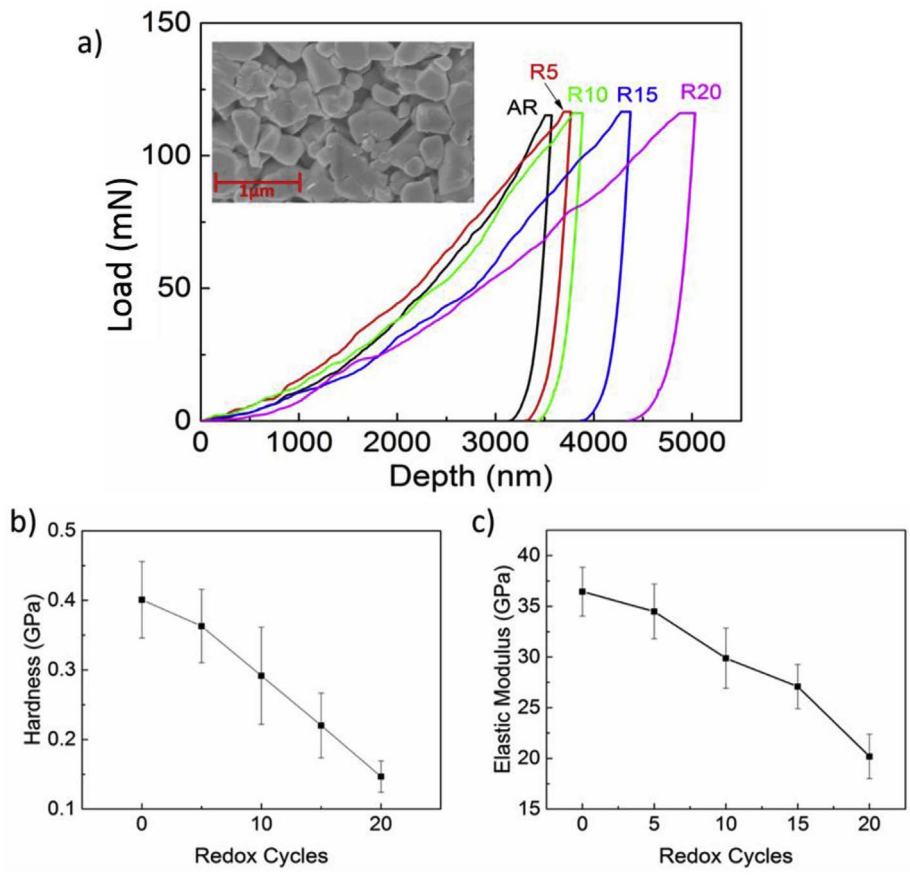


Fig. 7. a) Load-depth curves for Ni-YSZ anodes after different numbers of redox cycles as obtained from nanoindentation, the inset shows the area been indented on the as-reduced sample; b) Hardness vs. numbers of redox cycles for the tested Ni-YSZ anodes; c) and Elastic modulus vs. numbers of redox cycles for the tested Ni-YSZ anodes. The standard deviations are obtained statistically from over 200 measurements per sample.

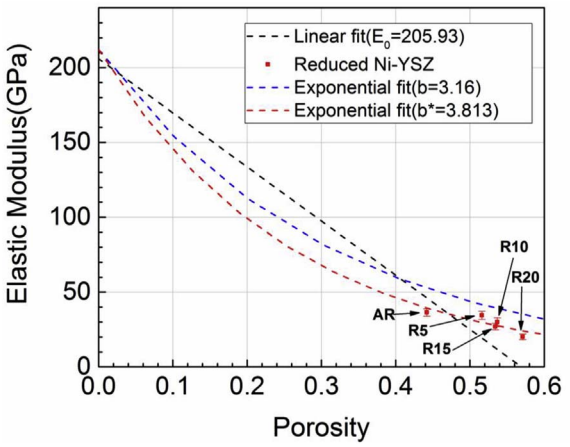


Fig. 8. Elastic modulus vs porosity of reduced samples. The results of fitting using exponential and free linear model are represented as blue and black lines, respectively, while the red line corresponds to the exponential fit with a different porosity constant. (For interpretation of the references to colour in this figure legend, the reader is referred to the web version of this article.)

Table 2
Linear and exponential correlations of elastic modulus vs porosity. E_0 is the elastic modulus of the fully dense material, b is a porosity constant and p is fractional porosity. b* is the porosity constant fitted in this study, considering the microstructure damage caused by redox cycling.

		E_0(GPa)	b
Linear	$E = E_0(1 - bp)$	205.93[29]	1.756
Exponential	$E = E_0 exp(-bp)$	212.1[27]	3.16
Exponential	$E = E_0 exp(-bp)$	212.1	3.813*

related to differences in the measuring techniques and input parameters as well as to the microstructural changes occurred during the redox cycling. In fact, redox cycling does not increase the porosity only, but it also leads to the internal YSZ framework break down, Ni agglomeration and change in pore shape, resulting in an elastic modulus smaller than that expected for non-redox cycled electrodes.

4. Conclusions

The electrochemical and mechanical deterioration of Ni-YSZ anodes after up to 20 redox cycles was quantified by a combination of FIB-SEM tomography, impedance spectroscopy, nanoindentation and modelling.

Upon redox cycling the hardness changes from 0.4 GPa to 0.15 GPa and the elastic modulus from 36.4 GPa to 20.2 GPa. This can be qualitatively associated to observations in the SEM: fractures at the YSZ grain boundaries, Ni-YSZ detachment, continuous nickel agglomeration and increasing porosity after each redox cycle, all of which seem to be irreversible. The effect of porosity in the mechanical properties can be suitably understood with the empirical elastic modulus-porosity exponential relation where only the porosity constant was re-fitted.

The electrochemical degradation was followed by impedance spectroscopy and a physically-based model was used to infer the active TPB length from the temporal evolution of the polarisation resistance, revealing a good matching with TPB density obtained through FIB-SEM tomography. In particular, the model fits very well the initial, 5 redox and 10 redox samples, with a less satisfactory fit for higher redox cycles due to the changes in the effective conductivity of the composite caused by YSZ fractures and nickel agglomeration. It is also observed that the polarisation resistance decreased temporarily by a factor ca. 2 upon each re-reduction, probably due to the transient generation of Ni nanoparticles around the TPB coming from the volume shrinkage from NiO to Ni. Although this causes a temporary decrease in polarisation resistance, after each redox cycle the degradation rate is even faster due to the promoted Ni agglomeration. This results in an overall increase in polarisation resistance by about an order of magnitude as a consequence of a reduction in active TPB density (from 4.63 μm^{-2} to 1.06 μm^{-2}) and fragmentation of the YSZ network along its grain boundaries due to Ni expansion upon oxidation.

This study shows that the microstructural changes during redox cycling are the primary cause of Ni-YSZ material degradation in both electrochemical performance and mechanical properties. The repeating Ni volume changes are the main cause of this degradation process, damaging the YSZ framework and reducing the TPB density as a consequence of accelerated Ni coarsening. The study further demonstrates that a comprehensive quantification of redox cycling can be achieved by coupling 3D tomography, real-time impedance spectroscopy and mechanical analysis.

Acknowledgements

This project has received funding from the China Scholarship Council, European Union's Horizon 2020 research and innovation programme under the Marie Skłodowska-Curie grant agreement No 654915 and EPSRC grant EP/M014045/1. Helpful discussions with Dr. Zhangwei Chen, Dr. Samuel J. Cooper, Dr. Farid Tariq and Mr. Mengzheng Ouyang are gratefully acknowledged.

References

[1] D. Sarantaridis, A. Atkinson, Redox cycling of Ni-based solid oxide fuel cell anodes: a review, Fuel Cells 7 (2007) 246–258.
[2] A. Faes, et al., RedOx study of anode-supported solid oxide fuel cell, J. Power Sources 193 (2009) 55–64.
[3] M. Hanasaki, et al., SOFC durability against standby and shutdown cycling, J. Electrochem. Soc. 161 (2014) 850–860.
[4] S. Tao, J.T.S. Irvine, A redox-stable efficient anode for solid-oxide fuel cells, Nat. Mater. 2 (2003) 320–323.
[5] J. Laurencin, G. Delette, O. Sicardy, S. Rosini, F. Lefebvre-Joud, Impact of 'redox' cycles on performances of solid oxide fuel cells: case of the electrolyte supported cells, J. Power Sources 195 (2010) 2747–2753.
[6] J.R. Wilson, et al., Three-dimensional reconstruction of a solid-oxide fuel-cell anode, Nat. Mater. 5 (2006) 541–544.
[7] A. Faes, A. Hessler-Wyser, D. Presvytes, C.G. Vayenas, J. Van herle, Nickel-Zirconia anode degradation and triple phase boundary quantification from microstructural analysis, Fuel Cells 9 (2009) 841–851.
[8] P. Tanasini, et al., Experimental and theoretical investigation of degradation mechanisms by particle coarsening in SOFC electrodes, Fuel Cells 9 (2009) 740–752.
[9] T. Shimura, Z. Jiao, S. Hara, N. Shikazono, Quantitative analysis of solid oxide fuel cell anode microstructure change during redox cycles, J. Power Sources 267 (2014) 58–68.
[10] M.H. Pihlatie, A. Kaiser, M. Mogensen, M. Chen, Electrical conductivity of Ni–YSZ composites: degradation due to Ni particle growth, Solid State Ionics 189 (2011) 82–90.
[11] D. Waldbillig, A. Wood, D. Ivey, Thermal analysis of the cyclic reduction and oxidation behaviour of SOFC anodes, Solid State Ionics 176 (2005) 847–859.
[12] M.S. Khan, et al., Fundamental mechanisms involved in the degradation of nickel-yttria stabilized zirconia (Ni-YSZ) anode during solid oxide fuel cells operation: a review, Ceram. Int. (2015), http://dx.doi.org/10.1016/j.ceramint.2015.09.006.
[13] J.R. Izzo, et al., Nondestructive reconstruction and analysis of SOFC anodes using X-ray computed tomography at Sub-50?nm resolution, J. Electrochem. Soc. 155 (2008) B504.
[14] J.R. Wilson, J.S. Cronin, S.A. Barnett, Linking the microstructure, performance and durability of Ni-yttria-stabilized zirconia solid oxide fuel cell anodes using three-dimensional focused ion beam–scanning electron microscopy imaging, Scr. Mater 65 (2011) 67–72.
[15] P.R. Shearing, et al., Exploring Microstructural Changes Associated with Oxidation in Ni–YSZ SOFC Electrodes Using High Resolution X-ray Computed Tomography, (2012), http://dx.doi.org/10.1016/j.ssi.2011.10.015.
[16] G. Brus, K. Miyoshi, H. Iwai, M. Saito, H. Yoshida, Change of an anode's microstructure morphology during the fuel starvation of an anode-supported solid oxide fuel cell, Int. J. Hydrogen Energy 40 (2015) 6927–6934.
[17] M. Kubota, T. Okanishi, H. Muroyama, T. Matsui, K. Eguchi, Microstructural evolution of Ni-YSZ cermet anode under thermal cycles with redox treatments, J. Electrochem. Soc. 162 (2015) F380–F386.
[18] O. Pecho, et al., 3D microstructure effects in Ni-YSZ anodes: influence of TPB lengths on the electrochemical performance, Mater. (Basel) 8 (2015) 7129–7144.
[19] C.A. Schuh, Nanoindentation studies of materials, Mater. Today 9 (2006) 32–40.
[20] H. Schichlein, A.C. Müller, M. Voigts, A. Krügel, E. Ivers-Tiffée, Deconvolution of electrochemical impedance spectra for the identification of electrode reaction

mechanisms in solid oxide fuel cells, J. Appl. Electrochem 32 (2002) 875–882.
[21] J.I. Gazzarri, O. Kesler, Electrochemical AC impedance model of a solid oxide fuel cell and its application to diagnosis of multiple degradation modes, J. Power Sources 167 (2007) 100–110.
[22] A. Lasia, Electrochemical Impedance Spectroscopy and its Applications, Springer, New York, 2014, http://dx.doi.org/10.1007/978-1-4614-8933-7.
[24] A. Bertei, et al., Validation of a physically-based solid oxide fuel cell anode model combining 3D tomography and impedance spectroscopy, Int. J. Hydrogen Energy 41 (2016) 22381–22393.
[25] J. Chen, A. Bertei, E. Ruiz-Trejo, A. Atkinson, N.P. Brandon, Characterization of degradation in nickel impregnated scandia-stabilize zirconia electrodes during isothermal annealing, J. Electrochem. Soc. 164 (2017) F935–F943.
[26] A. Bertei, et al., The fractal nature of the three-phase boundary: a heuristic approach to the degradation of nanostructured solid oxide fuel cell anodes, Nano Energy 38 (2017) 526–536.
[27] M. Radovic, E. Lara-Curzio, Mechanical properties of tape cast nickel-based anode materials for solid oxide fuel cells before and after reduction in hydrogen, Acta Mater 52 (2004) 5747–5756.
[28] J. Laurencin, G. Delette, B. Morel, F. Lefebvre-Joud, M. Dupeux, Solid oxide fuel cells damage mechanisms due to Ni-YSZ re-oxidation: case of the anode supported cell, J. Power Sources 192 (2009) 344–352.
[29] M. Pihlatie, A. Kaiser, M. Mogensen, Mechanical properties of NiO/Ni–YSZ composites depending on temperature, porosity and redox cycling, J. Eur. Ceram. Soc. 29 (2009) 1657–1664.
[30] A. Selcuk, A. Atkinson, Elastic properties of ceramic oxides used in solid oxide fuel C:ells (SOFC), J. Eur. Ceram. Soc. 17 (1997) 1523–1532.
[31] M. Radovic, E. Lara-Curzio, L. Riester, Comparison of different experimental techniques for determination of elastic properties of solids, Mater. Sci. Eng. A 368 (2004) 56–70.
[32] Z. Chen, N. Brandon, Inkjet printing and nanoindentation of porous alumina multilayers, Ceram. Int. 42 (2016) 8316–8324.
[33] Z. Chen, X. Wang, V. Bhakhri, F. Giuliani, A. Atkinson, Nanoindentation of porous bulk and thin films of La0.6Sr 0.4Co0.2Fe0.8O3-?? Acta Mater 61 (2013) 5720–5734.
[34] A. Bieberle, L.P. Meier, L.J. Gauckler, The electrochemistry of Ni pattern anodes used as solid oxide fuel cell model electrodes, J. Electrochem. Soc. 148 (2001) A646.
[35] J. Chen, A. Bertei, E. Ruiz-Trejo, A. Atkinson, N.P. Brandon, Characterization of degradation in nickel impregnated scandia-stabilize zirconia electrodes during isothermal annealing, J. Electrochem. Soc. 164 (2017) F935–F943.
[36] S.J. Cooper, A. Bertei, P.R. Shearing, J.A. Kilner, N.P. Brandon, TauFactor: an open-source application for calculating tortuosity factors from tomographic data, SoftwareX 5 (2016) 203–210.
[37] S. Gadag, G. Subbarayan, W. Barker, Thermo-elastic properties of dense YSZ and porous Ni-ZrO2 monolithic and isotropic materials, J. Mater. Sci. 41 (2006) 1221–1232.
[38] N.A.A. Sakharova, J.V.V. Fernandes, J.M.M. Antunes, M.C.C. Oliveira, Comparison between Berkovich, Vickers and conical indentation tests: a three-dimensional numerical simulation study, Int. J. Solids Struct. 46 (2009) 1095–1104.
[39] E. Ruiz-trejo, A. Atkinson, N.P. Brandon, Metallizing porous scaffolds as an alternative fabrication method for solid oxide fuel cell anodes, J. Power Sources 280 (2015) 81–89.
[40] Z. Jiao, N. Shikazono, Simulation of the reduction process of solid oxide fuel cell composite anode based on phase field method, J. Power Sources 305 (2016) 10–16.
[41] L. Holzer, et al., Microstructure degradation of cermet anodes for solid oxide fuel cells: quantification of nickel grain growth in dry and in humid atmospheres, J. Power Sources 196 (2011) 1279–1294.
[42] F. Tariq, et al., Advanced 3D imaging and analysis of SOFC electrodes, ECS Trans. 64 (2014) 81–86.
[43] F. Tariq, et al., 3D imaging and quantification of interfaces in SOFC anodes, J. Eur. Ceram. Soc. 34 (2014) 3755–3761.
[44] A. Bertei, J. Mertens, C. Nicolella, Electrochemical simulation of planar solid oxide fuel cells with detailed microstructural modeling, Electrochim. Acta 146 (2014) 151–163.
[45] D. Simwonis, H. Thülen, F.J. Dias, A. Naoumidis, D. Stöver, Properties of Ni/YSZ porous cermets for SOFC anode substrates prepared by tape casting and coat-mix process, J. Mater. Process. Technol. 92–93 (1999) 107–111.
[46] L. Holzer, et al., Redox cycling of Ni–YSZ anodes for solid oxide fuel cells: influence of tortuosity, constriction and percolation factors on the effective transport properties, J. Power Sources 242 (2013) 179–194.
[47] Y.-T. Cheng, C.-M. Cheng, Scaling, dimensional analysis, and indentation measurements, Mater. Sci. Eng. R. Rep. 44 (2004) 91–149.